Comparison of Bearingless Slice Motor Topologies for Pump Applications

P. Puentener,
M. Schuck,
D. Steinert,
J. W. Kolar

ETH
Eidgenössische Technische Hochschule Zürich
Swiss Federal Institute of Technology Zurich

Comparison of Bearingless Slice Motor Topologies for Pump Applications

P. Puentener, M.Schuck and J. W. Kolar
Power Electronic Systems Laboratory, ETH Zürich
Zürich, Switzerland
puentener@lem.ee.ethz.ch

D. Steinert
Levitronix GmbH
Zürich, Switzerland

Abstract—**This paper compares two bearingless slice motor topologies, namely the temple and slotless designs, with respect to the achievable motor efficiency for pump applications. Stator losses, passive stiffness properties and the achievable torque are determined by means of 3D FEM simulations. Some basic pump design guidelines are introduced and the expected motor performance is evaluated for typical operating conditions encountered in medical applications. It is shown that the temple design outperforms the slotless design in all but low pressure applications. Two prototypes, one radial and one axial pump, are manufactured by means of stereolitograpy 3D printing. The hydraulic characteristics of the designs are measured using the temple and slotless motor for the radial and the axial pump, respectively. The radial pump exhibits significantly higher pressure-numbers, while the axial design yields higher flow-numbers.**

Index Terms—**bearingless, temple topology, slotless topology, pump, medical application**

I. INTRODUCTION

The bearingless slice motor topology was introduced in [1] and can be applied in various applications, such as pumps, reaction-wheels, compressors, mixers and blowers [2]–[6]. In contrast to conventional active magnetic bearings (AMBs), bearingless motors do not feature a dedicated bearing unit. Instead, the drive and bearing units are integrated into the same magnetic (back iron) and electric (coils) circuits. Axial deflections as well as tilting movements of the rotor are passively stable if the rotor radius is significantly larger than its height, which leads to a compact motor design. Due to contactless levitation of the rotor, bearingless slice motors are well suited as pumps for medical applications. To date, several pumps featuring AMBs are commercially available [7]. All bearingless slice motors applied in this field rely on a stator in temple design, as introduced in [8]. In recent years, a novel bearingless motor topology without stator slots was developed based on the concept of a toroidally wound brushless DC motor [9], [10]. This so-called slotless bearingless motor features low stator losses at high rotational speeds [11].

In this work, the slotless topology is compared to the conventional temple design for pump applications in the medical field. The designs are compared at a nominal flow of $5\,\mathrm{l/min}$ and pressures in the range of $10-400\,\mathrm{mmHg}$ ($1.3-53\,\mathrm{kPa}$),

which covers a wide range of medical applications, such as cardiopulmonary or ventricular assist devices (CPAD or VAD), cardiopulmonary bypass (CPB) and extracorporeal life support (ECLS) [12], [13].

II. MOTOR TOPOLOGIES

The bearingless slice motor topologies considered in this work are illustrated in Fig. 1. Both topologies consist of drive and bearing coils that are wound around the stator iron. The drive torque and magnetic bearing forces are generated using the same magnetic circuit. The rotor consists of a flat, diametrically-magnetized permanent magnet ring.

The temple motor, as shown in Fig. 1(a), consists of L-shaped stator claws with windings that are wound along the axial direction. The magnetic path is closed by a ring-shaped stator back iron below the stator claws. The magnetic air gap is equivalent to the mechanical air gap, which provides sufficient space for the wall of a process chamber while maintaining a low magnetic reluctance of the air gap, resulting in high passive stiffnesses (see Section II-B). To date, bearingless pumps have been implemented using the temple topology as it provides a relatively large free space above the rotor that can be used for the pump head.

The slotless bearingless motor (see Fig. 1(b)) consists of a ring-shaped stator iron and toroidally wound drive and bearing coils. Due to the required winding window area passing through the air gap, the magnetic air gap is larger than the mechanical one. This results in lower passive stiffnesses for a given mechanical air gap length (e.g. for integrating a process chamber). The slotless design has been used in ventilation and compressor applications, which require high rotational speeds that would result in high harmonic stator losses in a temple topology (see Section II-D).

A. Rotor Field Distribution

The field that the rotor magnet generates in the magnetic air gap can be approximated by

$$\vec{B}_{\mathrm{PM}} = \hat{B}_{\mathrm{r}} \cos(\theta - \omega t)\vec{e}_{\mathrm{r}} + \hat{B}_{\mathrm{t}} \sin(\theta - \omega t)\vec{e}_{\theta}, \qquad (1)$$

where B_{r} and B_{t} denote the radial and tangential component of the magnetic flux density, respectively. At the equilibrium position of the rotor, the axial component of the magnetic flux density is negligibly small compared to its other components.
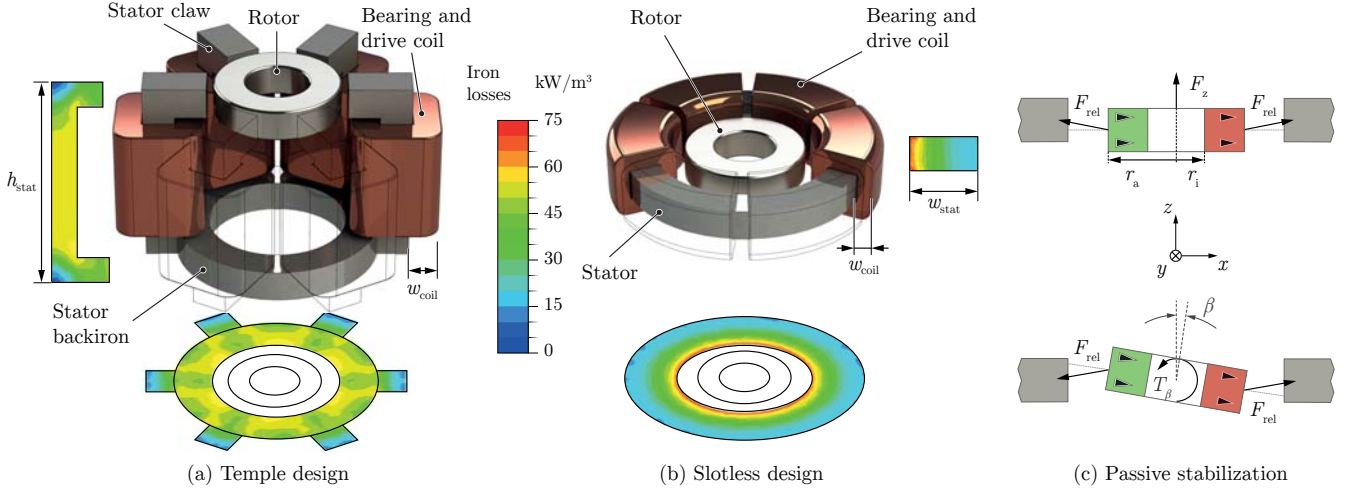
Fig. 1. Illustration of exemplary temple (a) and slotless (b) motor designs including the stator loss density at a rotational speed of $8\,000\,\mathrm{rpm}$. Illustration of the passive stabilizing forces (c). Refer to Section II-B and III for a detailed explanation.

B. Passive Characteristics

Due to the disk shape of the rotor (diameter $>>$ height), the rotor is passively stabilized in the axial and tilting directions. Deviations from the equilibrium point result in an increase of the magnetic reluctance, thus causing a restoring force. This is illustrated in Fig. 1(c).

The passive stiffnesses are commonly defined as:

$$c_x = -\frac{\mathrm{d}F_x}{\mathrm{d}x}, \quad c_y = -\frac{\mathrm{d}F_y}{\mathrm{d}y}, \quad c_z = -\frac{\mathrm{d}F_z}{\mathrm{d}z} \quad (2)$$

$$c_\alpha = -\frac{\mathrm{d}T_\alpha}{\mathrm{d}\alpha}, \quad c_\beta = -\frac{\mathrm{d}T_\beta}{\mathrm{d}\beta}, \quad (3)$$

where F_i and T_i represent the force in the i direction and torque around the i axis, respectively. The stiffnesses c_x and c_y are negative, corresponding to a passively unstable behavior. Thus, the radial position of the rotor has to be actively stabilized by means of magnetic forces.

C. Torque and Force Generation

To describe the torque and force generation, consider the slotless topology as depicted in Fig. 1(b). If the windings are excited by a current $i(\theta)$, the resulting Lorentz force density acting on the rotor can be expressed as

$$\vec{f} = i(\theta) \cdot (B_t \vec{e}_r - B_r \vec{e}_\theta), \quad (4)$$

where θ represents the azimuth and current is counted positive towards positive z-direction inside the air gap.

To obtain the resulting force and torque, one needs to integrate the force density along the circumference,

$$\vec{F}_{xy} = h_{rot} r_a \int_0^{2\pi} \vec{f}\,\mathrm{d}\theta = h_{rot} r_a \int_0^{2\pi} \mathbf{R} \cdot \begin{pmatrix} f_r \\ f_t \end{pmatrix} \mathrm{d}\theta \quad (5)$$

$$T_z = h_{rot} r_a \int_0^{2\pi} \left(\vec{r} \times \vec{f}\right) \mathrm{d}\theta = h_{rot} r_a^2 \int_0^{2\pi} f_t\,\mathrm{d}\theta \quad (6)$$

where

$$\mathbf{R} = \begin{pmatrix} \cos(\theta) & -\sin(\theta) \\ \sin(\theta) & \cos(\theta) \end{pmatrix} \quad (7)$$

and h_{rot} denote the rotational matrix and rotor height, respectively.

If the current is chosen as

$$i_{drv}(\theta) = \hat{I}\cos(\theta - \omega t - \theta_{drv}), \quad (8)$$

the resulting torque can be found as

$$T_z = h_{rot} r_a^2 \hat{B}_r \hat{I} \pi \cos(\theta_{drv}), \quad (9)$$

while the force densities in radial direction compensate each other and no resulting bearing force occurs.

If it is chosen as

$$i_{bng}(\theta) = \hat{I}\cos(2\theta - \omega t - \theta_{bng}), \quad (10)$$

no torque is generated and the radial force can be calculated as

$$\vec{F}_{xy} = \frac{\hat{I}(\hat{B}_r + \hat{B}_t)h_{rot} r_a \pi}{2} \begin{pmatrix} \cos(\theta_{bng}) \\ \sin(\theta_{bng}) \end{pmatrix}. \quad (11)$$

The desired current distribution can be achieved as the fundamental component of N equally distributed coils if they are excited according to

$$i_{drv,i} = \hat{I}_{drv} \cos\left(\frac{(i-1)2\pi}{N} - \omega t - \theta_{drv}\right) \quad i \in \{1, N\}, \quad (12)$$

and

$$i_{bng,i} = \hat{I}_{bng} \sin\left(2\frac{(i-1)2\pi}{N} - \omega t - \theta_{bng}\right) \quad i \in \{1, N\}. \quad (13)$$

D. Stator Harmonics

For a slotted stator, the magnetic flux density in the air gap is modulated depending on the geometry of the stator slots. In the temple topology, the 6 rectangular-shaped stator claws cause field harmonics of 5th and 7th order in addition to the purely sinusoidal field as generated by the rotor magnet. The harmonic content is especially high for the tangential field component. In the slotless topology, the uniformity of the stator shape results in an almost perfectly sinusoidal field distribution in the air gap and no field concentrations and modulations occur. The spectra of the magnetic flux density in the air gap is illustrated in Fig. 2 for a rotor angle of $\omega t = 0$ for both, the temple and slotless topologies.
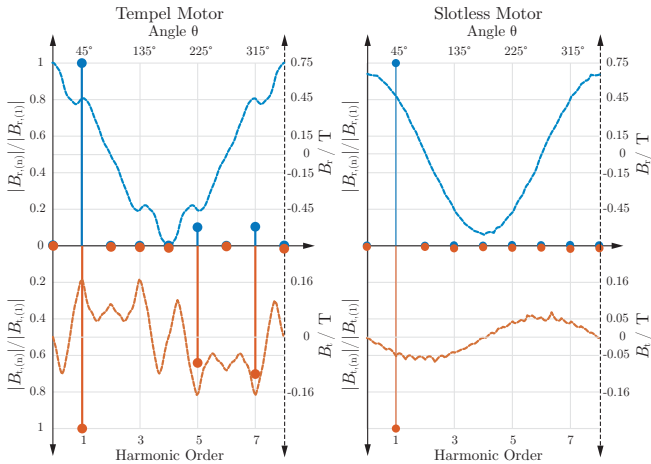
Fig. 2. Flux density and harmonic content of the radial B_r and tangential B_t components in the air gap for the temple (left) and slotless (right) motor topology.

III. MOTOR LOSSES

The overall motor losses are mainly composed of ohmic copper losses and stator losses. While the copper losses are proportional to the motor torque, the stator losses are mainly caused by the rotating magnetic field of the spinning rotor. Further losses, such as rotor losses, proximity losses in the stator windings, and other loss components caused by the PWM current ripple have been neglected in this work. PWM-related motor losses become negligible for high switching frequencies (low current harmonics). Proximity effects mainly occur for the slotless motor topology and can be reduced significantly by using litz wire for the windings [14].

A. Ohmic Losses

The ohmic losses can be calculated as

$$P_{cu} = RI^2 = \rho_{cu} l_{tot} A_{cu} J_{rms}^2, \tag{14}$$

where ρ_{cu}, l_{tot}, A_{cu}, and J_{rms} denote the resistivity of copper, the total wire length, the cross-sectional copper area, and the RMS current density, respectively. The temperature dependency of the resistivity is accounted for iteratively by using the thermal model presented below.

B. Iron Losses

Iron losses are composed of hysteresis and eddy current losses that are caused by the alternating magnetic field in the stator. As a first approximation, these losses can be modeled by the Steinmetz equation

$$P_{stat} = C_m \int_{V_{stat}} f^\alpha \hat{B}^\beta \, dV, \tag{15}$$

where the Steinmetz parameters C_m, α and β can be found by a robust least-square fit of the loss measurement data provided in the datasheet of the stator material. These parameters are listed in Table I for sheeted electrical steel M330-35A.

TABLE I
STEINMETZ PARAMETERS OF M330-35A

C_m	24.54 W/(m³Hz$^\alpha$T$^\beta$)
α	1.5
β	1.85

For the slotless topology, it is possible to approximate the stator losses by assuming a sinusoidal time dependency of the magnetic flux density in the stator iron. Since the B-field is approximately constant along the axial direction, it is sufficient to determine the peak flux density in the xy-plane as a function of the radius.

For the temple design, this is not easily possible because the flux density does not vary sinusoidally throughout the entire stator volume. Therefore, the stator losses have to be obtained using transient 3D FEM simulations.

To illustrate the distribution of the stator losses, Fig. 1 shows simulation results for the stator loss density caused by the rotor field for two exemplary machine designs with identical rotor diameter, magnetic air gap length, outer stator radius, and at the same rotational speed. The losses in the slotless topology occur mainly at the inner wall of the stator iron and are uniformly distributed in the axial and circumferential directions. Contrarily, loss peaks occur in the stator back iron between the stator teeth and within the claws in the temple design.

C. Thermal Model

The losses in the stator cause an increase of the machine temperature ϑ. The overall generated loss power P_{tot} has to be dissipated via the surface area A_{sur} of the machine by means of convection, advection, and thermal radiation. To evaluate the steady state temperature based on which the copper resistivity of the windings is obtained, a simplified thermal model is used in this work. Both topologies feature a cylindrical shape. It is, therefore, assumed that all motor losses have to be dissipated via the surface area of a vertically aligned cylinder. Heat transfer coefficients for such an arrangement have been presented in [15]. Losses in the rotor and the fluid in pump applications are dissipated by means of advection trough the pump outlet. The contacting walls between the pump head and the motor can thus be modeled as an adiabatic interface

(i.e. the rotor and pump losses do not contribute to the steady state temperature of the stator), as long as the flow rate is sufficiently high.

Consequently, the steady state temperature can be calculated using

$$P_{\text{stat}} = \alpha_{\text{th}} A_{\text{sur}} (\vartheta - \vartheta_{\text{amb}}), \tag{16}$$

where α_{th} and ϑ_{amb} denote the heat transfer coefficient and the ambient temperature, respectively. Since the ohmic losses P_{cu} and the heat transfer coefficient are temperature dependent, this equation has to be solved iteratively.

IV. PUMP DESIGN

A. Principles of Centrifugal Pumps

According to the Euler turbine equation

$$Y_{\text{th}} = u_2 v_{\text{u},2} - u_1 v_{\text{u},1}, \tag{17}$$

centrifugal pumps transfer the specific work Y to the fluid by increasing the product of the circumferential components of the absolute flow velocity v_{u} and the impeller blade speed u from the inlet (subscript 1) to the outlet (subscript 2). While this theoretical upper limit is easy to derive, the actual flow conditions inside the pump and the resulting hydraulic losses are difficult to assess. In general, the efficiency of a pump is reduced, the further away it is operated from its nominal operating point that is was designed for. Thus, to achieve a high hydraulic efficiency at a desired operating point, the impeller has to be carefully designed. A starting point for such a design it to attune the impeller speed to its diameter. This can be obtained from the Cordier diagram [16].

B. Design Requirements

The results of an empirical study that maps the best efficiency points of industrial pumps into a diagram of the dimensionless parameters

$$\delta_{\text{M}} = d_{\text{imp}} \frac{\sqrt{\pi}}{2} \frac{(2Y)^{1/4}}{Q^{1/2}}, \qquad \sigma_{\text{M}} = \frac{\omega}{\sqrt{\pi}} \frac{Q^{1/2}}{(2Y)^{3/4}} \tag{18}$$

have been published in [17]. Here, d_{imp} and Q represent the outer diameter of the impeller blade and the volumetric flow rate, respectively.

From Fig. 3, it can be found that the diameter number δ_{M} must decrease with increasing speed number σ_{M}. Furthermore, it can be seen that the impeller blade should be designed to extend in the radial direction for large diameter numbers, while axial pumps are preferable for high speed numbers.

For the considered motor designs, the flow must pass through the inner diameter of the rotor magnet if an axial pump design is chosen. As a result, the outer diameter of the impeller is significantly smaller than the rotor diameter ($d_{\text{imp}} < 2r_{\text{a}}$).
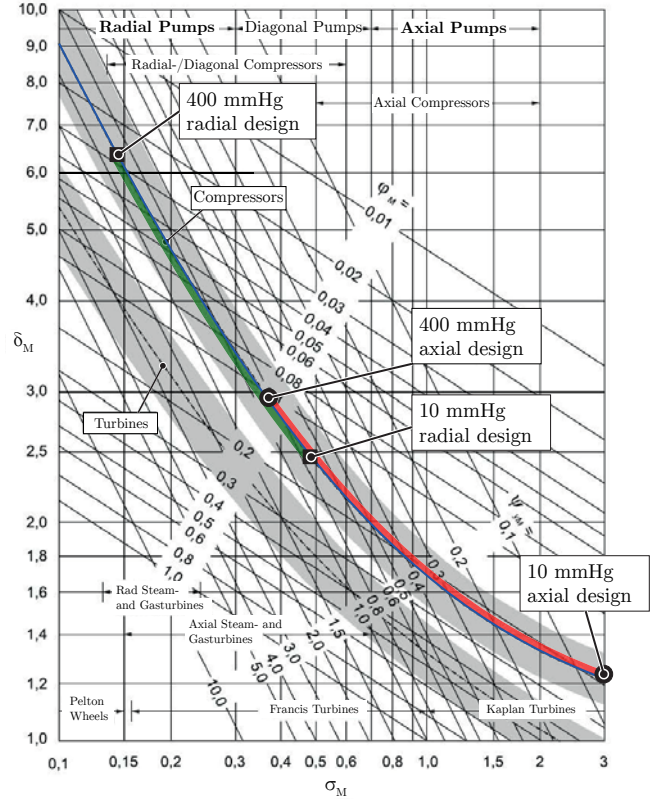
Fig. 3. Cordier diagram illustrating the optimal relation between the speed number σ_{M} and the diameter number δ_{m}. The range of simulated radial and axial designs is illustrated in green and red, respectively. Figure adapted from [16].

C. Hydraulic Efficiency

According to [18], it can be assumed that the maximum efficiency of a pump increases with increasing speed number σ_{M}. However, for such low flow volumes, efficiencies should not be expected to exceed $\eta_{\text{pump}} = 0.5$ [19]. Furthermore, for bearingless pumps, leakage flow through the radial gap of the bearing is significant and reduces the hydraulic efficiency. Therefore, a hydraulic efficiency of $\eta_{\text{pump}} = 0.4$ has been assumed over the entire range of speed numbers in the subsequent considerations. From the known hydraulic power $P_{\text{hyd}} = Q \cdot \Delta p$ and the assumed hydraulic efficiency, the required mechanical torque can be calculated as

$$T_{\text{mech}} = \frac{P_{\text{hyd}}}{\omega \cdot \eta_{\text{pump}}}. \tag{19}$$

D. Hydraulic Forces

During operation, the magnetic forces discussed in Section II have to counteract the occurring hydraulic forces, of which the axial thrust is the most critical as it is solely counteracted passively. For axial pump designs, complete compensation of the axial thrust is only possible at the nominal operating point of the pump. In this work, only axial pump designs that result in an axial deflection of the rotor of less than half of its height (i.e. $\delta_z < h_{\text{rot}}/2$) are considered feasible.

The rotor displacement for axial pumps is estimated as

$$F_{\mathrm{ax}} = \Delta p \cdot (r_{\mathrm{a}}^2 - r_{\mathrm{i}}^2)\pi = \delta_z \cdot c_z, \qquad (20)$$

where Δp, r_{a}, and r_{i} denote the pressure difference across the pump, the outer rotor radius, and the inner rotor radius, respectively.

E. Mechanical Airgap

The mechanical air gap has to be sufficiently large to accommodate the wall of a process chamber and further allow for some translatory movement of the rotor. For medical applications, large fluid gaps are desirable to reduce the destruction of blood cells [20]. In this work, the wall thickness of the process chamber was chosen as $w_{\mathrm{w}} = 0.5\,\mathrm{mm}$ to provide sufficient stability against pressure forces.

F. Iron Saturation

All 3D FEM simulations were conducted for M330-35A electrical steel sheet. Clearly, the iron losses and also saturation effects depend on the material properties. To achieve a fair comparison, both topologies were simulated with the same material.

According to the data-sheet, M330-35A reaches saturation around $B \approx 1.3\,\mathrm{T}$.

V. MOTOR OPTIMIZATION

The loss and thermal models presented in section III are used to determine the optimal stator dimensions. Fig. 4 represents the design procedure used to evaluate both topologies for a predefined hydraulic operating point. By defining the range of hydraulic operating conditions of interest and the choice of a magnet size, one can determine the required rotor speed from the Cordier diagram. Depending on whether the speed number suggests the implementation on an axial or radial impeller design, either the inner or outer radius of the magnet is chosen as the impellers outer diameter. Once the rotor size and speed is fully defined, iterations on various stator dimensions can be conducted. For the paper at hand, the mechanical air gap is fixed at $0.5\,\mathrm{mm}$ to ensure sufficient space for a process chamber that withstands the hydraulic pressure. Using 3D FEM simulations, the passive, active and loss characteristics of each design point was determined using magneto-static and transient simulations.

The required torque and thus the required drive current was calculated from the torque constant and equation (19).

While the stator losses result immediately from the simulations, the copper losses were determined by iterating the thermal mode until convergence was achieved.

A. Design Space

To limit the amount of parameters, the stator design space was limited to two variables for each topology, which were expected to significantly influence the motor efficiency, passive characteristics and power densities.

For the temple design, the coil width w_{coil}, the stator overall height h_{stat} were varied.
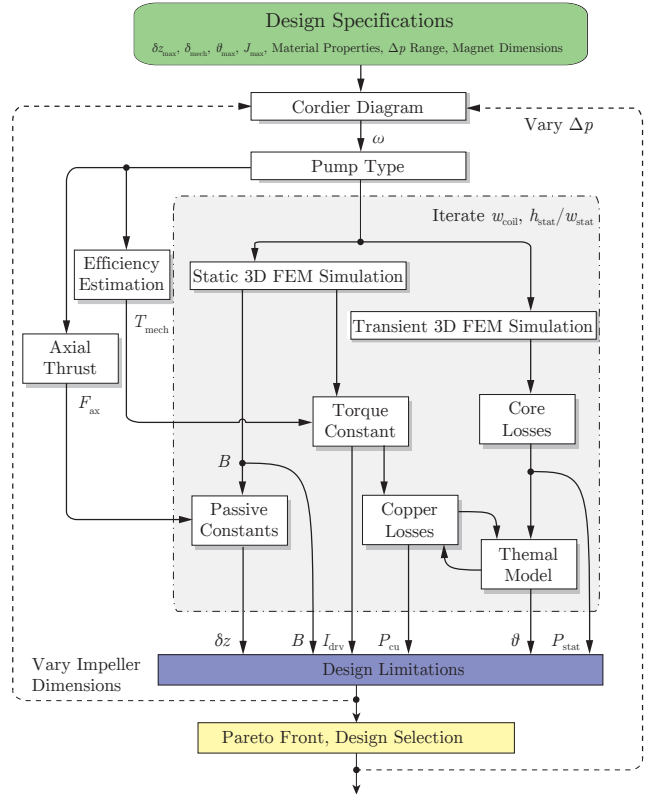
Fig. 4. Flow diagram illustrating the used design process to find optimal stator designs at given hydraulic operating conditions.

For the slotless topology, the coil width w_{coil} and the stator width w_{stat} was varied. The remaining dimensions were fixed or defined as a constant value of one of the other values.

For both topologies, variations of the magnet size were considered.

Table II lists the design space of the most important design parameters.

B. Evaluation

To evaluate the motor performance, the results of the design optimization were used to calculate the Pareto front between motor efficiency η_{mot} and hydraulic power density ρ_{hyd}. Fig. 5 exemplary illustrates the results for a slotless motor designed for an axial impeller with nominal pressure of $20\,\mathrm{mmHg}$.

TABLE II
DESIGN SPACE

Parameter	Variable	Temple	Slotless
Rotor Inner Diameter	r_{i}	$2.5 - 7.5\,\mathrm{mm}$	$2.5 - 7.5\,\mathrm{mm}$
Rotor Outer Diameter	r_{a}	$\{5, 10\}\,\mathrm{mm}$	$\{5, 10\}\,\mathrm{mm}$
Rotor Height	h_{rot}	$2.5 - 5\,\mathrm{mm}$	$2.5 - 5\,\mathrm{mm}$
Mechanical Air Gap	δ_{mech}	$0.5\,\mathrm{mm}$	$0.5\,\mathrm{mm}$
Coil Width	w_{coil}	$0.6 - 5\,\mathrm{mm}$	$0.2 - 7.5\,\mathrm{mm}$
Stator Height	h_{stat}	h_{rot}	$10 - 65\,\mathrm{mm}$
Claw Height	h_{claw}	$-$	h_{rot}

Due to the limited axial stiffness of the motor, the most efficient designs become infeasible. The hydraulic power density is mainly limited by saturation of the iron.
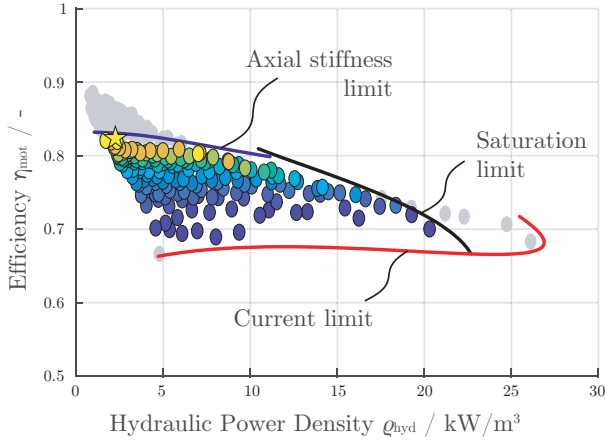
Fig. 5. Pareto front of an axial pump with slotless motor for an exemplary pressure difference of 20 mmHg. The color code indicates the magnet volume.

VI. TOPOLOGY COMPARISON

To compare the two motor concepts for pump applications, Fig. 6 illustrates the results for a rotor ring with an outer diameter of 20 mm and an inner diameter of 10 mm. Simulations were conducted for operating conditions on the Cordier line at pressures between $10 - 400$ mmHg (see Fig. 3).

For each combination of pump type, motor type and pressure difference, the motor efficiency versus power density Pareto front was determined. Figure 6 shows the design with highest motor efficiency for each topology for pressures between 10 mmHg and 400 mmHg.

It is found that the temple topology outperforms the slotless topology for radial impeller designs at all but low pressure conditions. For axial impellers, the slotless topology achieves higher motor efficiencies, due to the higher rotational speed required.

All these results assume that both impellers can be designed with equal efficiency of 40%.

VII. PROTOTYPES

To proof the concept of an axial pump and to compare the hydraulic characteristics, two impeller designs, an axial and a radial one were designed according to [21]. Nominal operation points were chosen as a flow rate of $5 \, \text{l/min}$ at a pressure difference of 50 mmHg and 400 mmHg, respectively.

Both pumps were constructed using a permanent magnetic ring with an outer and inner diameter of 20.5 mm and 12.5 mm, respectively. The impeller blades were constructed using a stereolithography 3D printer.

A photograph of the prototypes is shown in Fig. 7.

While the radial design was tested with a temple topology motor, the axial design was tested in a slotless topology. Both motors are shown in Fig. 7.
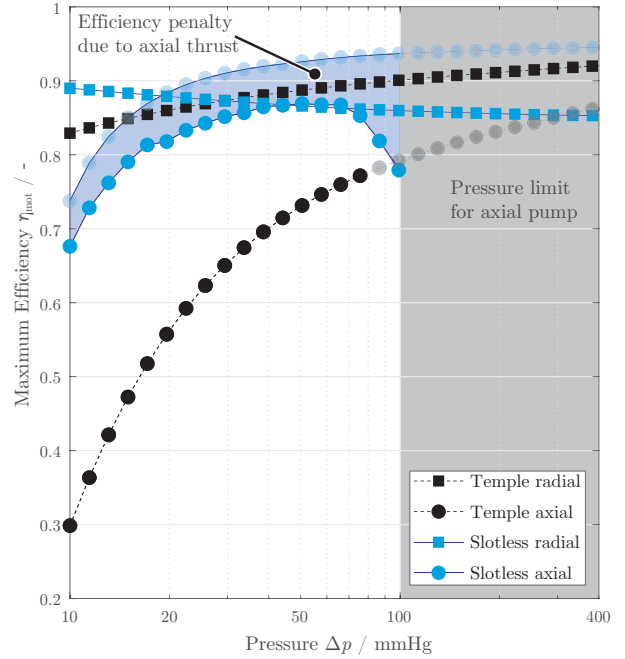
Fig. 6. Most efficient stator design for both topologies and impeller types. Pressures exceeding the maximum allowable value for axial designs are grayed-out. Slotless axial pumps suffer an efficiency penalty due to the limitation imposed by the passive axial stiffness.

VIII. MEASUREMENTS

The two pump concepts were tested on a hydraulic circuit filled with water. The fluid is pumped from a reservoir through tubing, back to the reservoir at constant rotor speed. To adjust the flow and pressure, a clamp valve at the high pressure side was used. The flow was measured using a clamp-on transducer. The pressure difference was measured 10 cm up- and downstream of the pump using manometers.

A. Hydraulic Characteristics

Both pumps achieve their nominal design points of $5 \, \text{l/min}$ at 50 mmHg and 400 mmHg pressure difference.

The pressure flow curves are illustrated in Fig. 8 and Fig. 9 for different rotational speeds.

The slotless topology achieves its nominal operating point at a rotational speed of approximately 19000 rpm. The maximum flow measured was $7.6 \, \text{l/min}$ at 36 mmHg. The shut-off pressure achieved was 64 mmHg.

The radial design shows a higher pressure capacity, as expected due to the larger impeller radius (r_a instead of r_i). The nominal operating point was achieved at 9000 rpm. Maximum flow measured was $16 \, \text{l/min}$ at 175 mmHg. Shut-off pressure at nominal speed was 475 mmHg.

To compare the two flow characteristics, Fig. 10 illustrates the curves in normalized form, as a function of the dimensionless parameters

$$\Phi = \frac{Q}{2\pi r_{\text{imp}}^2 b \omega} \qquad \text{and} \qquad \Psi = \frac{2Y}{(r_{\text{imp}}\omega)^2}, \qquad (21)$$
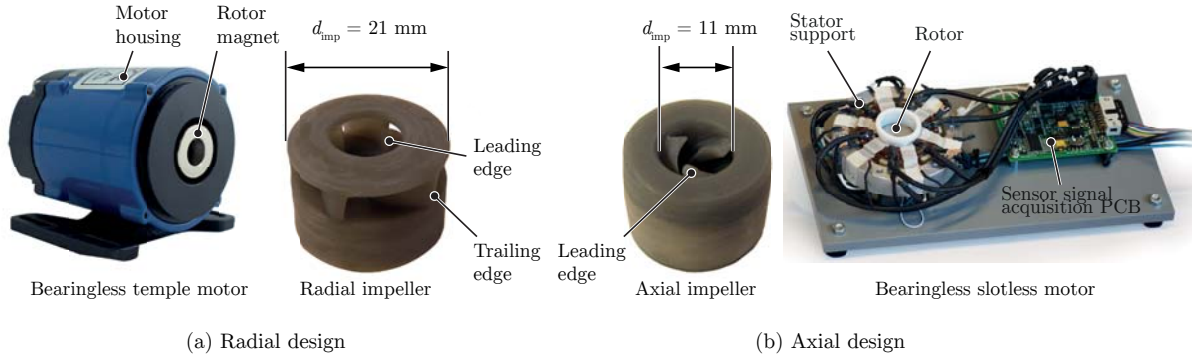
Fig. 7. Prototypes of the bearingless temple and slotless [22] motors together with 3D-printed prototypes of the impellers for $400\,\mathrm{mmHg}$ (a) and $50\,\mathrm{mmHg}$ (b).
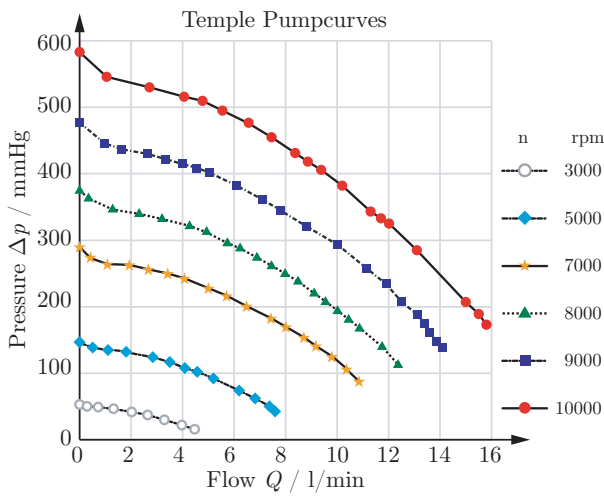
Fig. 8. Pressure and flow curve of the radial pump at rotational speeds between $2000 - 10000\,\mathrm{rpm}$.
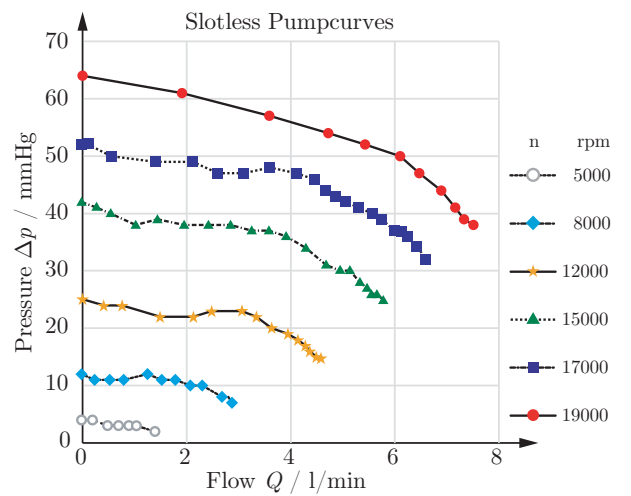
Fig. 9. Pressure and flow curve of the axial pump at rotational speeds between $5000 - 19200\,\mathrm{rpm}$.

where Φ, Ψ and b represent the flow-number, pressure-number and the blade height, respectively.

The radial pump achieves higher pressure-numbers Ψ at lower flow-numbers Φ. The dependency between these parameters is much stronger than for the axial pump. The axial pump achieves an almost constant pressure-number and achieves twice the flow-number.

IX. CONCLUSION

Two bearingless motor concepts, namely the temple and slotless topology, have been presented and compared. A design procedure was presented that can be used to determine the motor efficiency and power density for pumping applications. It was found by means of 3D FEM simulations that both concepts are suitable to be used as pumps.

Within the range of typical medical conditions of $10 - 500\,\mathrm{mmHg}$ pressure difference at $5\,\mathrm{l/min}$ flow, the two topologies were compared using 3D FEM simulations and the loss models presented.

It was found that the temple design is better suited for high pressure, low flow applications. These tend to be radial impeller designs, i.e. pumps with a low specific speed.

The slotless topology shows lower stator losses and is thus best suited for high speed applications. As a result, this topology is preferably applied in high flow, low pressure applications, i.e. pumps with a high specific speed and an axial impeller design.

One axial and one radial design were manufactured using a stereolithoraphic printer to prove the concept and to determine the flow and pressure characteristics. The pumps were operated with an slotless and temple motor, respectively.

As designed, the axial pump achieved an pressure difference of $50\,\mathrm{mmHg}$ at nominal flow. The required rotational speed was $19000\,\mathrm{rpm}$.

The radial pump achieves far higher hydraulic pressures. The nominal point of $400\,\mathrm{mmHg}$ pressure difference at $5\,\mathrm{l/min}$ flow was achieved at $9000\,\mathrm{rpm}$.
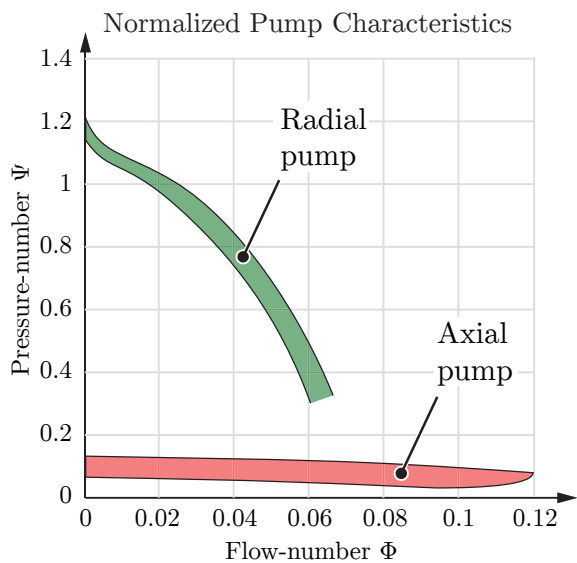
Fig. 10. Range of the normalized pump characteristics measured for the axial and radial pump.

REFERENCES

[1] R. Schoeb and N. Barletta, "Magnetic bearing. Principle and application of a bearingless slice motor." *JSME International Journal Series C Mechanical Systems, Machine Elements and Manufacturing*, vol. 40, no. 4, pp. 593–598, 1997.

[2] M. Neff, N. Barletta, and R. Schoeb, "Bearingless centrifugal pump for highly pure chemicals," in *Proc. 8th ISMB*, 2002, pp. 283–287.

[3] J. Zhou and K. J. Tseng, "A disk-type bearingless motor for use as satellite momentum-reaction wheel," in *Power Electronics Specialists Conference, 2002. pesc 02. 2002 IEEE 33rd Annual*, vol. 4, 2002, pp. 1971–1975.

[4] H. Mitterhofer, B. Mrak, and W. Amrhein, "Suitability investigation of a bearingless disk drive for micro turbine applications," in *Energy Conversion Congress and Exposition (ECCE), 2013 IEEE*. IEEE, 2013, pp. 2480–2485.

[5] B. Warberger, R. Kaelin, T. Nussbaumer, and J. W. Kolar, "50- /2500-W bearingless motor for high-purity pharmaceutical mixing," *IEEE Transactions on Industrial Electronics*, vol. 59, no. 5, pp. 2236–2247, May 2012.

[6] R. Baumschlager, R. Schoeb, and J. Schmied, "Bearingless hydrogen blower," in *Proc. on 8th ISMB Int. Symposium on Magnetic Bearings*, 2002.

[7] H. Hoshi, T. Shinshi, and S. Takatani, "Third-generation blood pumps with mechanical noncontact magnetic bearings," *Artificial organs*, vol. 30, no. 5, pp. 324–338, 2006.

[8] N. Barletta and R. Schoeb, "Design of a bearingless blood pump," *Proc. 3rd Int. Symp. on Magnetic Suspension Technology*, pp. 265–274, jul 1995.

[9] L. W. Langley and R. L. Fisher, "Toroidally wound brushless dc motor," Oct. 15 1985, uS Patent 4,547,713.

[10] H.-I. Lee, S.-y. Yoo, and M. D. Noh, "Toroidally-wound self-bearing bldc motor with lorentz force," *IEEE Transactions on Magnetics*, vol. 46, no. 6, pp. 2148–2151, 2010.

[11] H. Mitterhofer, D. Andessner, and W. Amrhein, "Analytical and experimental loss examination of a high speed bearingless drive," in *Power Electronics, Electrical Drives, Automation and Motion (SPEEDAM), 2012 International Symposium on*. IEEE, 2012, pp. 146–151.

[12] M. Rodefeld, "The fontan circulation: Time for a moon shot?" *The Journal of thoracic and cardiovascular surgery*, vol. 156, no. 1, pp. 252–253, 2018.

[13] T. V. Brogan, L. Lequier, R. Lorusso, G. MacLaren, and G. J. Peek, *Extracorporeal Life Support: The ELSO Red Book*. Extracorporeal Life Support Organization, 2017.

[14] D. Steinert, I. Kovacevic-Badstübner, T. Nussbaumer, and J. W. Kolar, "Loss investigation of slotless bearingless disk drives," in *2015 IEEE Energy Conversion Congress and Exposition (ECCE)*, Sept 2015, pp. 4418–4424.

[15] VDI-Gesellschaft Verfahrenstechnik und Chemieingenieurswesen, *VDI Heat Atlas*, 2nd ed. Springer Berlin Heidelberg, 2010.

[16] J. Seume and R. Mailach, "Grundlagen der strömungsmaschinen," in *Dubbel*. Springer, 2017, pp. 1289–1383.

[17] O. Cordier, "Ähnlichkeitsbedingungen für strömungsmaschinen," *BWK das Energie-Fachmagazin Verein Deutscher Ingenieure*, vol. 5, no. 10, pp. 337–340, oct 1953.

[18] R. Neumaier, "Hermetic pumps," *Houston, TX: Gulf Publishing Company*, 1997.

[19] A. J. Stepanoff, *Centrifugal and axial flow pumps: theory, design, and application*. Wiley New York, 1957.

[20] R. Kosaka, M. Nishida, O. Maruyama, T. Yambe, K. Imachi, and T. Yamane, "Effect of a bearing gap on hemolytic property in a hydrodynamically levitated centrifugal blood pump with a semi-open impeller," *Bio-medical materials and engineering*, vol. 23, no. 1-2, pp. 37–47, 2013.

[21] J. F. Gülich, *Centrifugal pumps*. Springer, 2008, vol. 2.

[22] P. Puentener, M. Schuck, D. Steinert, T. Nussbaumer, and J. W. Kolar, "A 150000 rpm bearingless slice motor," *IEEE/ASME Transactions on Mechatronics*, 2018.